



**HAL**  
open science

## Mesoscale structure, mechanics, and transport properties of source rocks' organic pore networks

Jérémie Berthonneau, Amaël Obliger, Pierre-Louis Valdenaire, Olivier Grauby, Daniel Ferry, Damien Chaudanson, Pierre Levitz, Jae Jin Kim, Franz-Josef Ulm, Roland J.-M. Pellenq

### ► To cite this version:

Jérémie Berthonneau, Amaël Obliger, Pierre-Louis Valdenaire, Olivier Grauby, Daniel Ferry, et al.. Mesoscale structure, mechanics, and transport properties of source rocks' organic pore networks. Proceedings of the National Academy of Sciences of the United States of America, 2018, 115 (49), pp.12365-12370. 10.1073/pnas.1808402115 . hal-02004400

**HAL Id: hal-02004400**

**<https://hal.science/hal-02004400>**

Submitted on 1 Feb 2019

**HAL** is a multi-disciplinary open access archive for the deposit and dissemination of scientific research documents, whether they are published or not. The documents may come from teaching and research institutions in France or abroad, or from public or private research centers.

L'archive ouverte pluridisciplinaire **HAL**, est destinée au dépôt et à la diffusion de documents scientifiques de niveau recherche, publiés ou non, émanant des établissements d'enseignement et de recherche français ou étrangers, des laboratoires publics ou privés.



# Mesoscale structure, mechanics, and transport properties of source rocks' organic pore networks

Jeremie Berthonneau<sup>a,1,2</sup>, Amaël Obliger<sup>a,1</sup>, Pierre-Louis Valdenaire<sup>a</sup>, Olivier Grauby<sup>b</sup>, Daniel Ferry<sup>b</sup>, Damien Chaudanson<sup>b</sup>, Pierre Levitz<sup>c</sup>, Jae Jin Kim<sup>d</sup>, Franz-Josef Ulm<sup>e</sup>, and Roland J.-M. Pellenq<sup>a,b,e</sup>

<sup>a</sup>MultiScale Material Science for Energy and Environment (<MSE><sup>2</sup>), Massachusetts Institute of Technology, Cambridge, MA 02139; <sup>b</sup>CNRS, UMR 7325, Aix-Marseille Université, Centre Interdisciplinaire de Nanoscience de Marseille (CINaM), 13288 Marseille Cedex 9, France; <sup>c</sup>CNRS, UMR 8234, Université Pierre et Marie Curie, Physicochimie des Electrolytes et Nanosystèmes Interfaciaux (PHENIX), 75252 Paris Cedex 5, France; <sup>d</sup>Shell Technology Center at Houston, Shell International Exploration and Production Inc., Houston, TX 77082; and <sup>e</sup>Department of Civil and Environmental Engineering, Massachusetts Institute of Technology, Cambridge, MA 02139

Edited by Michael L. Klein, Temple University, Philadelphia, PA, and approved October 18, 2018 (received for review May 15, 2018)

**Organic matter is responsible for the generation of hydrocarbons during the thermal maturation of source rock formation. This geochemical process engenders a network of organic hosted pores that governs the flow of hydrocarbons from the organic matter to fractures created during the stimulation of production wells. Therefore, it can be reasonably assumed that predictions of potentially recoverable confined hydrocarbons depend on the geometry of this pore network. Here, we analyze mesoscale structures of three organic porous networks at different thermal maturities. We use electron tomography with subnanometric resolution to characterize their morphology and topology. Our 3D reconstructions confirm the formation of nanopores and reveal increasingly tortuous and connected pore networks in the process of thermal maturation. We then turn the binarized reconstructions into lattice models including information from atomistic simulations to derive mechanical and confined fluid transport properties. Specifically, we highlight the influence of adsorbed fluids on the elastic response. The resulting elastic energy concentrations are localized at the vicinity of macropores at low maturity whereas these concentrations present more homogeneous distributions at higher thermal maturities, due to pores' topology. The lattice models finally allow us to capture the effect of sorption on diffusion mechanisms with a sole input of network geometry. Eventually, we corroborate the dominant impact of diffusion occurring within the connected nanopores, which constitute the limiting factor of confined hydrocarbon transport in source rocks.**

porous media | electron tomography | mechanics | fluid transport | mesoscale

The emergence of disruptive technology (1, 2) in the field of petroleum engineering has improved access to hydrocarbons from source rock formations. As a result, the historically declining production of natural gas has been on the rise. The stimulation technique of hydraulic fracturing aims to create a fracture network accessing the hydrocarbons and to force their migration to the crack's surface (2, 3). However, as the bimodal production curves suggest, the large-scale deployment of hydraulic fracturing wells has led to invariably declining heterogeneous production rates (4–6). Early stages of these rates follow a square root of time drop, which in the long term becomes an exponential decay leading to limited production. The production of hydraulic fracturing wells depends on three factors: the capacity of creating fracture networks successfully reaching the confined hydrocarbons, the ability of maintaining these fractures opened, and the fluid transport properties of the materials storing hydrocarbons (4–7). At the molecular scale, hydrocarbons are generated within organic agglomerates—typically referred to as kerogens—composed of an amorphous porous carbon skeleton and dispersed in a fine-grained mineral matrix (7). The chemical composition of the carbon skeleton (carbon hybridization, functional groups) is known to evolve through thermal maturation induced during geological burial (8, 9). It is therefore imperative to establish a

deep scientific understanding of the structural, mechanical, and confined fluid transport properties of these organic agglomerates with respect to their thermal maturation. This type of knowledge would allow predictions of the displacement of confined hydrocarbons from the organic matter to fracture networks and their contribution in the production of hydraulic fracturing wells.

Realistic atomistic-scale models of kerogens have begun being utilized to simulate hybridization of the carbon skeletons upon maturation (8). These chemical transitions strengthen the kerogen matrix and shift the rupture mechanism from a plastic to the brittle state. In addition, the structural arrangement of nanopores is responsible for their strong adsorption, the breakdown of continuum hydrodynamics, and the occurrence of interfacial wetting effects in agreement with the fast productivity declines of exploitation wells (10, 11). Such nanostructures demonstrate a self-diffusion governed transport regime (12). These recent breakthroughs, however, only account for the subnanopores network reached through atomistic-scale models (8). The presence of hierarchical structures of organic hosted pores evolving through thermal maturation, as probed in scanning electron microscopy (5, 13), small-angle neutron scattering (14–17), and adsorption (3, 14, 18), may affect the overall properties. For example, at an experimental macroscopic scale, the organic porosity has been found to be responsible for a significant reduction of the kerogen particle modulus with respect to thermal

## Significance

**In source rocks, natural hydrocarbons are generated from organic matter dispersed in a fine-grained mineral matrix. The potential recovery of hydrocarbons is therefore influenced by the geometry of the organic hosted porous networks. Here, the three-dimensional structures of such networks are revealed using electron tomography with a subnanometer resolution. The reconstructions are first characterized in terms of morphology and topology and then used to build a multiscale simulation tool to study the mechanics and the transport properties of confined fluids. Our results offer evidence of the prevalent role of connected nanopores, which subsequently constitutes a material limit for long-term hydrocarbon production.**

Author contributions: J.B., A.O., P.-L.V., O.G., F.-J.U., and R.J.-M.P. designed research; J.B., A.O., and P.-L.V. performed research; D.C., P.L., and J.J.K. contributed new reagents/analytic tools; J.B., A.O., P.-L.V., O.G., and D.F. analyzed data; and J.B., A.O., P.-L.V., and R.J.-M.P. wrote the paper.

The authors declare no conflict of interest.

This article is a PNAS Direct Submission.

This open access article is distributed under [Creative Commons Attribution-NonCommercial-NoDerivatives License 4.0 \(CC BY-NC-ND\)](https://creativecommons.org/licenses/by-nc-nd/4.0/).

<sup>1</sup>J.B. and A.O. contributed equally to this work.

<sup>2</sup>To whom correspondence should be addressed. Email: [berthonneau@cinam.univ-mrs.fr](mailto:berthonneau@cinam.univ-mrs.fr).

This article contains supporting information online at [www.pnas.org/lookup/suppl/doi:10.1073/pnas.1808402115/-DCSupplemental](https://www.pnas.org/lookup/suppl/doi:10.1073/pnas.1808402115/-DCSupplemental).

Published online November 15, 2018.

maturation (19). In addition, the analysis of gas adsorption isotherms demonstrates that thermal maturity of the organic matter affects the surface area, pore volume, and geometrical permeability (3, 14, 18, 20). However, any interpretation of adsorption data is restricted by the simplistic assumptions adopted in the models. The issue thus becomes the validity of results from both theoretical and experimental studies, which cannot be reliable without an accurate determination of geometrical arrangements of the organic pore networks at relevant scales (21).

Recent developments of bright-field electron tomography allow imaging pores of amorphous materials with sizes above 0.5 nm in three dimensions (21, 22). Such resolution overlaps with atomistic-scale models and permits a consistent multiscale approach. In this paper, we provide 3D reconstructions of the organic pore network of one oil-prone and two gas-prone source rocks with subnanometer resolution. We show that the parameters extracted from the analysis of the tomograms compare reasonably well to those measured with N<sub>2</sub> adsorption isotherms. This approach therefore offers an insight on the evolution of the organic pore networks in terms of structural, mechanical, and fluid transport properties at different thermal maturities. We demonstrate that the structural evolution affects not only an average pore radius and geometric surface area, but more importantly the tortuosity and connectivity. Through imaging informed simulation procedure, we further reveal that these topological features impact both mechanical and transport properties. We show that the mesoscale a maturation-induced decrease of rigidity. This offset the strengthening of carbon matrix as noted through reactive potential atomistic-scale models (8). In addition, following the previous work in this field (23–25), we study the influence of pressurized fluid inside pore networks, which leads to different stress distributions that impact crack nucleation areas. Combined with the recent findings on hydrocarbon transport within atomistic simulations of nanostructures (10–12), our analysis allows us to capture the effect of sorption on diffusion mechanisms with just a single input of the porous network geometry. As a conclusion, we show how the diffusion, occurring in the connected nanopores, constitutes the limiting factor of confined hydrocarbon transport, despite the consideration of sorption. The multiscale simulation approach presented here hence provides a way to access the interplay between topology and physical properties of porous solids at the mesoscale.

## Results

We first performed adsorption isotherms on three samples from economically valuable source rock formations containing type II kerogens: Marcellus (MAR), Haynesville (HAY), and Lower Eagle Ford (LEF). The organic geochemistry of these samples (*SI Appendix, Table S1*) plotted in the modified Van Krevelen diagram (26) illustrates their differences in terms of hydrocarbon generation potentials (*SI Appendix, Fig. S1B*). In brief, LEF is a source rock entering the oil window whereas HAY and MAR are source rocks in the dry gas window. The specific surface areas ( $A_s$ ), pore volumes ( $V_p$ ), and hydraulic radii ( $r_H$ ) obtained from N<sub>2</sub> adsorption analyses are summarized in *SI Appendix, Table S2*. The specific surface area increases with thermal maturity, which leads to decrease in the average pore size ( $r_H = 4V_p/A_s$ ) (*SI Appendix, Fig. S1C*). This aligns with previous studies performed on extended sets of shale gas plays (3, 14, 17). These results suggest that (i) the geothermal maturation (transition from oil-prone to gas-prone) triggers the formation of organic hosted nanopores (3, 13) and (ii) our source rocks samples correspond to the two extremes of this general tendency.

To further test this hypothesis, we performed direct observations and analysis of the pore networks. Among the organic agglomerates dispersed in source rocks, the migrated organic matter (solid bitumen and/or pyrobitumen) is recognized as the main contributor of organic hosted porosity (13). Focused ion beam (FIB) thin sections were extracted on those locations in each sample and their tridimensional structures were reconstructed through electron

tomography (*SI Appendix*). Fig. 1 *A–C* shows the tridimensional pore aperture maps of the electron tomograms of LEF, HAY, and MAR, respectively. Significantly different structures are readily observable, as evidenced by the decreasing ranges of aperture radii. The resulting pore-size distributions (PSDs), plotted in Fig. 1*D*, confirm this qualitative description. LEF presents a convex PSD with pore radii in the range of 3–12.6 nm, while HAY and MAR expose concave distributions dominated by nanopores ( $0.5 < r < 2.0$  nm). It is worth noting that our field of view precludes the observation of pore with  $r > 20$  nm, which impacts the PSD. Nonetheless, these distributions agree with previous findings that present decrease of the average pore size (*SI Appendix, Fig. S1C*) with respect to thermal maturity (3, 13, 14).

The in-pore chord length distribution (CLD) is recognized as an effective stereological tool for characterizing disordered porous media (27–29). The endpoints of frequency distribution segments appear at the pore interface,  $f_p(r)$ , and therefore were computed within the tomograms (Fig. 1*E*). LEF showed a constant distribution below 1 nm, which decreases slightly in the range of 1–11 nm, followed by a sharp decay. In HAY and MAR, the distributions are constant at  $r < 1.5$  nm and exhibit abrupt decays at larger values of  $r$ . The specific surface area,  $A_s$ , can be extracted from the first moment of the in-pore CLD using the following equation (28):

$$A_s = \frac{4\varphi_{meso}}{\rho_s(1 - \varphi_{meso}) \langle \ell \rangle}, \quad [1]$$

where  $\varphi_{meso}$  is the porosity of the tomogram,  $\rho_s$  is the density of the solid phase, and  $\langle \ell \rangle$  is the first moment of the normalized CLD. The porosity ( $\varphi_{meso}$ ) was measured by the ratio of pore volume with the total volume of the tomogram. The density of the amorphous carbon matrix ( $\rho_s$ ) was arbitrarily estimated as  $\rho_s = 1.0$  g/cm<sup>3</sup> for LEF and  $\rho_s = 1.4$  g/cm<sup>3</sup> for HAY and MAR (8). If  $A_s$  is plotted as a function of the shortest chord length  $r_c$  (Fig. 1*F*), then the geometrical surface area ( $S^{geo}$ ) can be defined by extrapolating  $r_c$  to zero (29) using Eq. 2:

$$A_s = \frac{S^{geo}}{\alpha r_c + 1}, \quad [2]$$

where the constant  $\alpha$  equals 1.15, 0.55, and 0.95 nm<sup>-1</sup> for LEF, HAY, and MAR, respectively. From this expression, we obtain  $S^{geo} = 113$  m<sup>2</sup>/g for LEF, 217 m<sup>2</sup>/g for HAY, and 338 m<sup>2</sup>/g for MAR, which is in a reasonable agreement with values measured in gas adsorption experiments (*SI Appendix, Table S2*). Small discrepancies between specific surface areas obtained from adsorption isotherms and geometrically determined values were previously documented for mesoporous materials and evaluated at ~20% (30), with  $S^{geo}$  being greater than  $A_s$ . Despite the differences between two approaches, the results confirm the increase of accessible surface area as a function of thermal maturity and the predominance of subnanopores in MAR and HAY with respect to LEF. This decrease in average pore size can be reasonably related to the development of subnanopores within the organic agglomerate as it is converted to mobile alkanes such as methane (3).

One advantage of the 3D porous network reconstructions is the ability to directly measure their topological properties. The tortuosities calculated from random walkers traveling through pore networks were  $1.9 \pm 0.7$ ,  $3.7 \pm 0.5$ , and  $6.6 \pm 0.7$  for LEF, HAY, and MAR, respectively (*SI Appendix, Fig. S3*). These mean values increase with thermal maturity, whereas their SDs are related to the variance in PSD (31). Other studies have previously demonstrated that the geometrical permeability,  $k$ , ( $k = \varphi r_H^2/\xi$ ) of organic porous networks increases with maturity (3) [where  $\xi$  is the Kozeny dimensionless constant determined

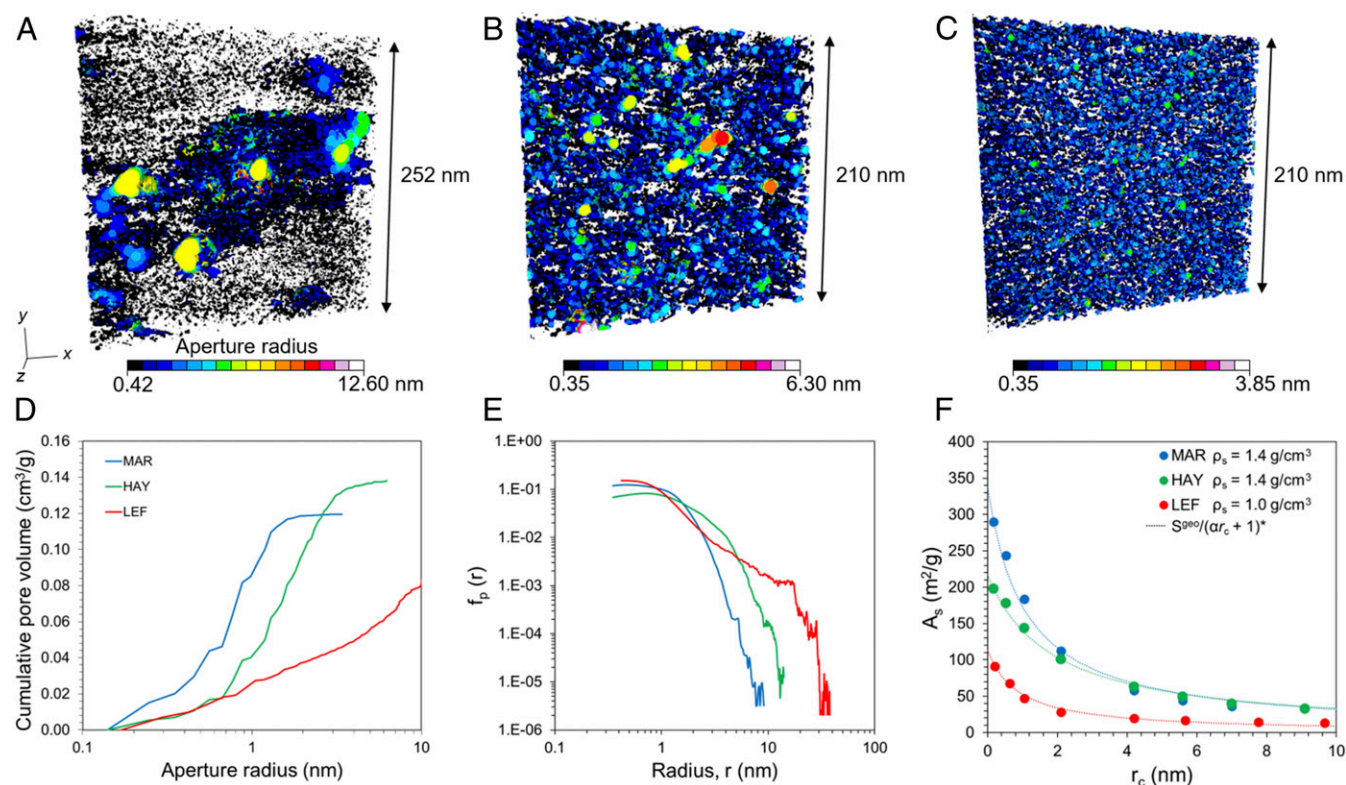


**Fig. 1.** Morphological characterization of the organic mesoporous networks imaged in electron tomography. Aperture maps of the organic pore networks of (A) LEF ( $\phi_{\text{meso}} = 9.1\%$ ), (B) HAY ( $\phi_{\text{meso}} = 19.3\%$ ), and (C) MAR ( $\phi_{\text{meso}} = 16.9\%$ ). (D) Pore-size distributions from aperture maps calculation. (E) In-pore CLDs. (F) Specific surface areas ( $A_s$ ) calculation from Eq. 1 as a function of the cutoff distance ( $r_c$ ) of the in-pore C.L.D.

from flow core plug experiments (32)]. The evolution of permeability was interpreted as the result of a significant decrease in tortuosity (reduction of  $\xi$  by a factor of 4–8). Contradictory to previous findings, we show that the tortuosity measured on the organic porous network of three source rocks increases with thermal maturity (*SI Appendix, Fig. S3*). In parallel, the connectivity density ( $\zeta$ ), obtained with the ratio of the first Betti number and the total volume of the tomogram (33), increase with maturity (*SI Appendix, Fig. S3*). This trend also rationalizes the differences observed between  $S^{\text{geo}}$  and  $A_s$  at low maturity (LEF), where a significant part of the pore network is disconnected and thus inaccessible to  $\text{N}_2$  molecules. This indicates that the thermal evolution of the organic matter not only entails morphological changes of the porous network (decreasing of  $r_H$  and concomitant increasing of  $S^{\text{geo}}$ ) as shown previously (3, 14), but it also implies major topological changes toward increasingly connected networks. We emphasize that these topological features impact the porosity detected in transmission electron microscopy, including organic nanopores ( $r < 1$  nm) that mainly connect the organic mesopores ( $r > 1$  nm).

The next step is to utilize a numerical approach to study the mechanical behavior and the confined hydrocarbons transport at the mesoscale. Lattice models were created by converting voxels of the binarized tomograms to lattice nodes corresponding to void, if porosity is detected, and the organic carbon skeleton (8). The mechanical, transport, and thermodynamical properties of the organic carbon skeleton presented hereafter take into account results from molecular dynamics using realistic numerical models of kerogen (8).

We used a fast Fourier transform (FFT)-based numerical method (34–36) to compute the elastic response of the lattice models from LEF and MAR (*SI Appendix, Eq. S3*). We arbitrarily assigned to the organic carbon skeleton a local Young's

modulus of 2 GPa for LEF and 15 GPa for MAR with a Poisson's ratio of 0.25 for both, in agreement with published data from molecular simulations on oil-prone (37) and gas-prone kerogens (8). Assuming the same Poisson's ratio at the box scale, the global Young's moduli resulting from the simulations are 1.4 GPa and 6.9 GPa for LEF and MAR, respectively. Considering the linear elasticity, the ratio between macro- and micro-Young's moduli (i.e., the decrease of rigidity) constitutes the main relevant quantity. It comes to 70% for LEF and down to 46% for MAR. Since the porosity alone cannot explain this difference, we argue that the mesopore's topology is responsible for such decreases. The presence of a homogeneous and highly disordered porous network (Fig. 1C) therefore explains the counterintuitive link between the rigid organic carbon skeleton (8) of the gas-prone sample (MAR) and its flexible behavior at the upper scale. On the contrary, the oil-prone sample (LEF) presents a lower decrease in rigidity at the macroscopic scale due to heterogeneous distribution of pores, including isolated mesopores (Fig. 1A). This decrease of rigidity with thermal maturity is confirmed by experimental indentations (19).

In Fig. 2, we illustrate how the elastic energy is stored inside two mesostructures under agent (a), corresponding to an imposed averaged strain  $\langle \epsilon_{ii} \rangle = 0.01$ , and agent (b), including an adsorbed fluid characterized by a fluid pressure  $P$ . The total elastic energy, reduced per volume unit ( $10^6$  J/m<sup>3</sup>), is 0.82 for LEF-(a), 0.9 for LEF-(b), 4.13 for MAR-(a), and 4.5 for MAR-(b). For (a) and (b) we observe a similar total stored energy for a given averaged strain. However, agent (a) leads to Gaussian energy distributions, whereas agent (b) leads to exponential energy distributions (Fig. 2). These two types of distributions have already been established in porous networks where it was shown that exponential distributions govern the crack initiation zones (38). This demonstrates that the pressurized fluid, not studied by classical tensile tests, is critical in predicting the mechanical

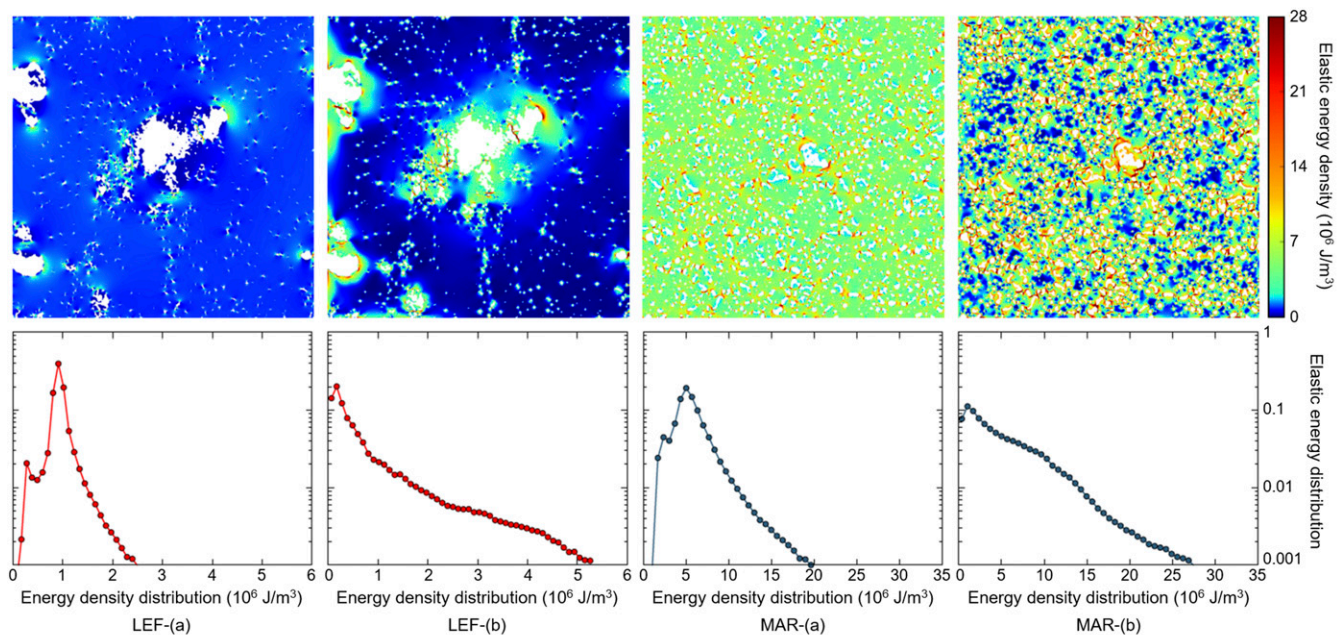


**Fig. 2.** Elastic simulations of the two porous mesostructures originating from LEF and MAR under two types of agent: (a) imposed strain boundary, and (b) adsorbed fluid with free strain boundary. The averaged strain of the simulation box is  $\langle \epsilon_{ij} \rangle = 0.01$  for all cases. The size is  $700 \times 700$  pixels with a resolution of 0.42 nm for LEF and 0.35 nm for MAR. Mesopore phase is in white. (Top) Elastic energy density fields ( $10^6 \text{ J/m}^3$ ). (Bottom) Distribution of the elastic energy density ( $10^6 \text{ J/m}^3$ ) for each simulation.

damage of organic matter contained in source rocks. In fact, hydraulic fracture propagation is directly influenced by stress distribution as crack nucleation appears more likely in high elastic energy areas. It corresponds to the vicinity of the largest pores for LEF-(b), leaving the rest of the matter undamaged. Contrary, crack nucleation can be more homogeneous at higher thermal maturity [see Fig. 2, MAR-(b)].

We applied the continuous time random walk (CTRW) (39–42) algorithm to study the confined hydrocarbons transport properties over the geometry given by the mesoscale lattice models. The

numerical scheme used here to simulate transport consists of constructing random walks, where walkers can move isotropically on the lattice. Because two different diffusion timescales are considered, one for each phase (i.e., the nanoporous and the mesoporous phases), we also assign random transit times at each step of the random walk from exponential distributions characterized by an average transit time that depends on the phase where the walker is located. To account for sorption between nano- and mesoporous phases, we use partial boundary conditions at the interface (see *SI Appendix* for more details on the homogenization

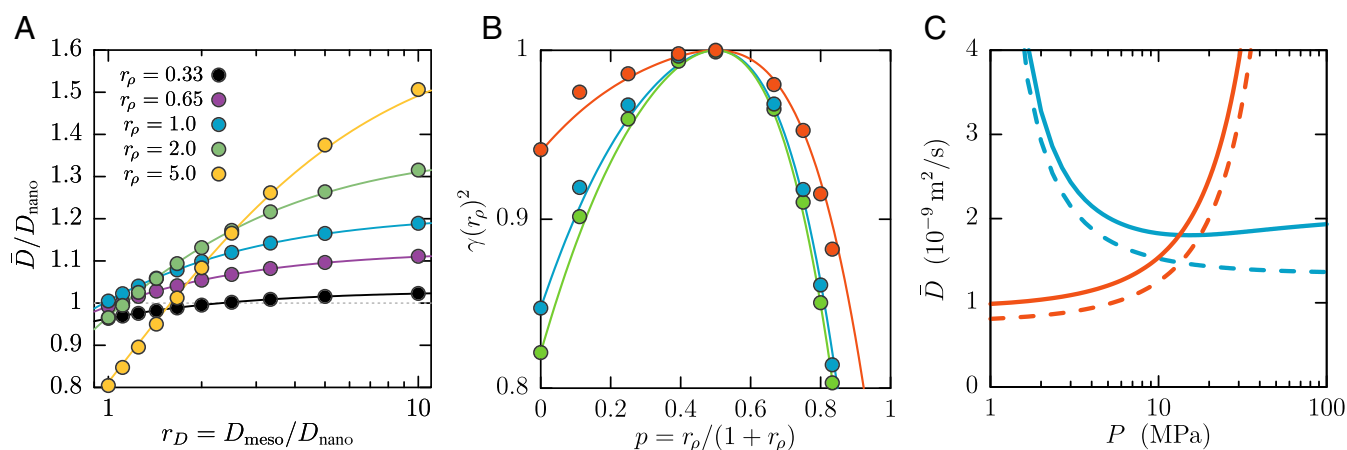


**Fig. 3.** Homogenized fluid transport properties of the mesoscale lattice models. (A) Homogenized diffusion coefficient of the MAR reconstruction scaled by  $D_{\text{nano}}$  as function of the diffusion contrast  $r_D = D_{\text{meso}}/D_{\text{nano}}$  for different concentration ratios  $r_\rho = \rho_{\text{meso}}/\rho_{\text{nano}}$  indicated by colors. The corresponding curves stand for the effective medium theory (Eq. 2) where the value of  $\gamma(r_\rho)^2$  is  $\bar{D}/D_{\text{nano}}$  when  $D_{\text{meso}} = D_{\text{nano}}$  (i.e.,  $r_D = 1$ ). (B) Concentration-dependent obstruction factor  $\gamma(r_\rho)^2$  as function of the probability  $p(r_\rho)$  for a random walker to cross the interface from the nano- to the mesoporous phase (red: LEF, green: HAY, blue: MAR). The corresponding curves display the analytical model (Eq. 4) where  $\gamma_0^2$  is simply taken as  $\gamma_0^2 = \gamma(p=0)^2$ . (C) Homogenized diffusion coefficient of methane for LEF (red) and MAR (blue) as function of the bulk fluid pressure. The dashed curves correspond to the diffusion in the nanoporous phase only, while the solid lines represent the homogenized model with mesoporosity. Standard geological conditions ( $T = 400 \text{ K}$  and lithostatic pressure of 25 MPa) have been considered.

procedure). Due to limited size of the mesopores and their connectivity through the nanoporous phase, where transport has been shown to be purely diffusive (10, 12, 42), we neglect advection in the system. Moreover, the amorphous nature of the nanoporous phase would prevent hydrodynamic slip at the interface. As a result, we treat both phases as homogeneous, which means that we attribute a single fluid concentration  $\rho_i$  and diffusion coefficient  $D_i$  per phase. Fig. 3A shows the homogenized diffusion coefficient,  $\bar{D}$ , adimensionned by  $D_{nano}$  as function of the diffusion ratio  $r_D = D_{meso}/D_{nano}$  in the MAR case for various concentration ratios  $r_\rho$ . We observe that the upscaled diffusion coefficient increases with the diffusion ratio. We use an effective medium theory (EMT) (43, 44) to rationalize the dependence on  $r_D$  as

$$\frac{\bar{D}}{D_{nano}} = \frac{1 + r_\rho r_D}{1 + r_\rho r_D^{-1}} \gamma(r_\rho)^2, \quad [3]$$

where  $r_\rho = \varphi/(1 - \varphi)$  is the ratio of the volume fractions of the mesoporous phase ( $\varphi$ ) and the nanoporous phase ( $1 - \varphi$ ), and  $\gamma(r_\rho)^2$  is an obstruction factor that captures the impact of geometry and sorption at the interface on the homogenized diffusion coefficient. Fig. 3A reports an excellent agreement between numerical results and the EMT where  $\gamma(r_\rho)^2$  is taken as  $\bar{D}(r_D=1)/D_{nano}$  for each curve. We notice that the influence of sorption depends nonmonotonically on the concentration ratio that controls the sorption effect.

Fig. 3B displays, for LEF, HAY, and MAR, an evolution of the obstruction factor ( $\gamma^2$ ) as a function of,  $p = r_\rho/(1 + r_\rho)$ , the probability of a random walker crossing an interface from nano- to mesoporous phase. When  $P = 0$  (or  $\rho_{meso} = 0$ ) there is no fluid in the mesopores;  $\gamma(p=0)^2 = \gamma_0^2$  is a constant that corresponds to the obstruction factor of the nanoporous phase, while the mesopores are considered as an impermeable phase. In practice, this can be computed by a simple random-walk simulation with bounce-back rules at the interface. If the concentration in mesopores increases and the probability  $p$  stays below 0.5, the diffusion increases due to an increased probability of the fluid entering mesopores. In this regime the fluid can use the mesopores as shortcuts, thus lowering the influence of the tortuosity of the nanoporous phase on the overall diffusion. When  $p$  gets closer to 0.5, the efficiency of the shortcut effect reaches a maximum because the decreasing probability of exiting from a mesopore balances the advantage of entering it. At  $p = 0.5$ , there is no influence of the interface because the probability of crossing the interface in both directions is the same, thus resulting in  $\gamma = 1$ . Beyond this point ( $p > 0.5$ ), mesopores start to act as traps because the probability of entering a mesopore becomes larger than the probability of escaping it. The homogenized diffusion coefficient thus diminishes and ultimately goes to zero in the limit of perfect trapping ( $p = 1$  or  $r_\rho \rightarrow \infty$ ). An analytical model (SI Appendix) for the concentration-dependent obstruction factor becomes

$$\gamma(p)^2 = \frac{\gamma_0^2 + 4(1 - \gamma_0^2)p(1 - p) + p^3 \sqrt{4(1 - \gamma_0^2)} 4p(1 - p)}{1 + p^3 \sqrt{4(1 - \gamma_0^2)}}. \quad [4]$$

Fig. 3B shows an excellent agreement between the proposed model and numerical results. For three very different geometries, the model (Eq. 4) captures the effect of sorption on diffusion through  $p$  with only one parameter  $\gamma_0^2$ , which depends on the geometry of the system.

We then compare, in Fig. 3C, the diffusion coefficient in a single nanoporous phase with the one accounting for the distribution of mesopores given by the tomograms as a function of pressure  $P$  of bulk methane in mesopores. For the diffusion coefficient in the nanoporous phase, we use a free volume theory. The methane concentration in the nanoporosity is given by a Langmuir

adsorption isotherm. Transport and adsorption behaviors in subnanopores for MAR were obtained by molecular simulation studies using the atomistic-scale model of Marcellus (8, 45). As a first approximation, we treat methane in mesopores as a bulk fluid. Bulk properties of methane, diffusion coefficient, and concentration as a function of  $P$  are taken from the National Institute of Standards and Technology database. For the MAR case, diffusion at low pressure is dominated by the nanoporous phase because of the strong heat of adsorption of nanopores due to confinement effects. Then, instead of decreasing exponentially with pressure, the diffusion model that accounts for mesopores reaches a minimum around 15 MPa and increases at higher pressure to become almost constant when  $P$  approaches 100 MPa (Fig. 3C). Consequently, the recovery of confined hydrocarbons is impacted at the mesoscopic level by nonmonotonic evolution of transport properties in time. We also report the same quantities in the LEF case but with diffusion in the nanoporous phase described by a more general free-volume model that accounts for adsorption-induced swelling (SI Appendix), which leads to an exponential increase as a function of pressure (46, 47). Due to swelling, the adsorption isotherm evolves linearly with  $P$  (until  $P > 50$  MPa) (48), thus lowering the impact of sorption on transport at the mesoscale. As a result, mesopores do not induce a qualitative change on the transport behavior at the mesoscale. Quantitatively, in both cases, the application of the CRTW algorithm showed that the transport of confined hydrocarbons at the mesoscale is mainly dictated by the nanoporosity. If mesopores in the gas-prone (rigid) case can induce nonmonotonical trend for the diffusion coefficient, they do not induce that effect for the oil-prone case (flexible nanoporosity). At the engineering scale, these trends complement the effect of fractures on wells' productivity. As already pointed out in previous studies (49–51), the pressure dependence of fractures' permeability can lead to a decrease of productivity when pressure decreases. The diffusion mechanisms evidenced here would either accentuate the productivity decrease for oil-prone organic matter, or partially mitigate it for gas-prone organic matter.

## Discussion

Bright-field electron tomography was applied on source rocks' organic matter, which allowed 3D reconstructions of the organic porous networks with a subnanometer resolution. Structural analysis of the tomograms demonstrated that thermal maturation entails increase of the accessible surface area, tortuosity, and connectivity of the nanoporous networks. Lattice models were then produced using the coupling between (i) geometrical arrangements of the porous networks at the mesoscale with (ii) nanoscale features deduced from a molecular dynamics study (8). These models allowed studying numerically an elastic response and the confined hydrocarbons transport properties at the mesoscale. Our results highlight the effect of topological changes on the organic matter rigidity. Moreover, we showed that pressurized fluid inside pore networks implies different potential crack nucleation areas, localized around the largest pores for the oil-prone case (LEF), and more homogeneously distributed at higher thermal maturity (MAR). The dominant impact of diffusion mechanisms occurring within the nanoporosity on confined hydrocarbon transport, previously sensed through atomistic studies, was also confirmed at the mesoscale. The constraint from imaging allowed a relatively simple computation of the only two parameters required by the fluid transport model: the volume fraction of the mesoporosity and the obstruction factor  $\gamma_0^2$  of the nanoporous phase. These results have also led to some questions, specifically whether the evidenced mesoscale effects may be generalized to a larger ensemble of source rocks, and whether one can identify the key geochemical parameters of the thermal history triggering the

evolution. To conclude, the herein constructed analytical model can be readily used for predictions of “in-place” confined hydrocarbon recovery in multiscale approaches accounting for macropores, organic/inorganic interfaces, and fracture networks (52–54). This further improves the link between nanoscale constitutive models of porous materials (8, 10–12) and their engineering applications (4–6).

## Materials and Methods

This study was conducted on samples from economically valuable source rock formations (MAR, HAY, and LEF). The thermal maturity was evaluated by RockEval pyrolysis and standard organic petrology technique. Low-pressure N<sub>2</sub> isotherms were performed at 77 K using a Micromeritics 3Flex. Thin sections of organic inclusions were extracted in an FEI Helios NanoLab 660 FIB. Electron tomography acquisitions were carried out with a transmission electron microscope (JEOL JEM 2011) fitted with a LaB<sub>6</sub> electron gun, under a 200-kV accelerating voltage, and assisted by the Digital Micrograph software (GATAN). The structural characterization was performed using iMorph

([imorph.sourceforge.net](http://imorph.sourceforge.net)) and imageJ. Lattice models were then created by converting voxels of the tomograms to lattice nodes. An FFT-based numerical model was used to compute the elastic response under two different agents: (i) an imposed averaged strain, and (ii) an adsorbed fluid inside pores. The CTRW algorithm was finally used to study the transport properties over the geometry of the lattice models (see *SI Appendix* for complementary details on *Materials and Methods*).

**ACKNOWLEDGMENTS.** We thank Jacob Michael Sobstyl [Massachusetts Institute of Technology (MIT)-Civil and Environmental Engineering] for his help regarding the manuscript. This work has been carried out within the framework of the ICoME2 Labex (ANR-11-LABX-0053) and the A\*MIDEX/Aix-Marseille University projects (ANR-11-IDEX-0001-02) cofunded by the French program “Investissements d’Avenir” managed by the ANR, the French National Research Agency. We acknowledge funding from Royal Dutch Shell and Schlumberger through the MIT X-Shale Hub as well as from Total through the MIT/CNRS FASTER-Shale project. We also thank Micromeritics Instrument Corp. for the generous gift of the 3Flex adsorption equipment.

- Kerr RA (2010) Energy. Natural gas from shale bursts onto the scene. *Science* 328:1624–1626.
- Cueto-Felgueroso L, Juanes R (2013) Forecasting long-term gas production from shale. *Proc Natl Acad Sci USA* 110:19660–19661.
- Valenza JJ, Drenzek N, Marques F, Pagels M, Mastarlerz M (2013) Geochemical controls on shale microstructure. *Geology* 41:611–614.
- Monteiro PJM, Rycroft CH, Barenblatt GI (2012) A mathematical model of fluid and gas flow in nanoporous media. *Proc Natl Acad Sci USA* 109:20309–20313.
- Silin D, Kneafsey T (2012) Shale gas: Nanometer-scale observations and well modelling. *J Can Pet Technol* 51:464–475.
- Patzek TW, Male F, Marder M (2013) Gas production in the Barnett shale obeys a simple scaling theory. *Proc Natl Acad Sci USA* 110:19731–19736.
- Vandenbroucke M, Largeau C (2007) Kerogen origin, evolution and structure. *Org Geochem* 38:719–833.
- Bousige C, et al. (2016) Realistic molecular model of kerogen’s nanostructure. *Nat Mater* 15:576–582.
- Tissot B, Welte D (1984) *Petroleum Formation and Occurrence* (Springer, Berlin).
- Falk K, Coasne B, Pellenq R, Ulm F-J, Bocquet L (2015) Subcontinuum mass transport of condensed hydrocarbons in nanoporous media. *Nat Commun* 6:6949.
- Lee T, Bocquet L, Coasne B (2016) Activated desorption at heterogeneous interfaces and long-time kinetics of hydrocarbon recovery from nanoporous media. *Nat Commun* 7:11890.
- Obliger A, Pellenq R, Ulm F-J, Coasne B (2016) Free volume theory of hydrocarbon mixture transport in nanoporous materials. *J Phys Chem Lett* 7:3712–3717.
- Louks RG, Reed RM, Ruppel SC, Jarvie DM (2009) Morphology, genesis, and distribution of nanometer-scale pores in siliceous mudstones of the Mississippian Barnett shale. *J Sediment Res* 79:848–861.
- Clarkson CR, et al. (2013) Pore structure characterization of North American shale gas reservoirs using USANS/SANS, gas adsorption, and mercury intrusion. *Fuel* 103:606–616.
- Mastarlerz M, He L, Melnichenko YB, Rupp JA (2012) Porosity of coal and shale: Insights from gas adsorption and SANS/USANS techniques. *Energy Fuels* 26:5109–5120.
- Thomas JJ, Valenza JJ, Craddock PR, Bake KD, Pomerantz AE (2013) The neutron scattering length density of kerogen and coal as determined by CH<sub>3</sub>OH/CD<sub>3</sub>OH exchange. *Fuel* 117:801–808.
- Gu X, et al. (2016) Quantification of organic porosity and water accessibility in Marcellus shale using neutron scattering. *Energy Fuels* 30:4438–4449.
- Wang Y, Zhu Y, Chen S, Li W (2014) Characteristics of the nanoscale pore structure in Northwestern human shale gas reservoirs using field emission scanning electron microscopy, high-pressure mercury intrusion, and gas adsorption. *Energy Fuels* 28:945–955.
- Zargari S, Wilkinson TM, Packard CE, Prasad M (2016) Effect of thermal maturity on elastic properties of kerogen. *Geophysics* 81:M1–M6.
- Happel J, Brenner H (1983) *Low Reynolds Number Hydrodynamics* (Martinus Nijhoff, Boston).
- Stoekel D, et al. (2014) Morphological analysis of disordered macroporous-mesoporous solids based on physical reconstruction by nanoscale tomography. *Langmuir* 30:9022–9027.
- Biermans E, Molina L, Batenburg KJ, Bals S, Van Tendeloo G (2010) Measuring porosity at the nanoscale by quantitative electron tomography. *Nano Lett* 10:5014–5019.
- Perkins TK, Kern LR, Aime M (1961) Widths of hydraulic fractures. *J Pet Technol* 13:937–949.
- Heider Y, Markert B (2017) A phase-field modeling approach of hydraulic fracture in saturated porous media. *Mech Res Commun* 80:38–46.
- Peng S, et al. (2018) Hydraulic fracture simulation with hydro-mechanical coupled discretized virtual internal bond. *J Petrol Sci Eng* 169:504–517.
- Van Krevelen DW (1961) *Coal: Typology, Chemistry, Physics, Constitution* (Elsevier, Amsterdam).
- Mering J, Tchoubar D (1968) Interprétation de la diffusion centrale des rayons X par les systèmes poreux. *J Appl Cryst* 1:153–165.
- Pellenq RJ-M, Levitz P (2002) Capillary condensation in a disordered mesoporous medium: A grand conical Monte Carlo study. *Mol Phys* 100:2059–2077.
- Ioannidou K, et al. (2016) Mesoscale texture of cement hydrates. *Proc Natl Acad Sci USA* 113:2029–2034.
- Coasne B, Galarneau A, Di Renzo F, Pellenq RJ-M (2010) Molecular simulation of nitrogen adsorption in nanoporous silica. *Langmuir* 26:10872–10881.
- Gostovic D, Smith JR, Kundinger DP, Jones KS, Wachsmann ED (2007) Three-dimensional reconstruction of porous LSCF cathodes. *Electrochem Solid State Lett* 10:B214–B217.
- Ozgunus T, Mobedi M, Ozkol U (2014) Determination of Kozeny constant based on porosity and pore to throat size ratio in porous medium with rectangular rods. *Eng Appl Comput Fluid Mech* 8:308–318.
- Odgaard A, Gundersen HJG (1993) Quantification of connectivity in cancellous bone, with special emphasis on 3-D reconstructions. *Bone* 14:173–182.
- Moulinec H, Suquet P (1995) A FFT-based numerical model for computing the mechanical properties of composites from images of their microstructures. *IUTAM Symposium on Microstructure-Property Interactions in Composites Materials* (Springer, Dordrecht, The Netherlands), pp 235–246.
- Moulinec H, Suquet P (1998) A numerical method for computing the overall response of nonlinear composites with complex microstructures. *Comput Methods Appl Mech Eng* 157:69–94.
- Schneider M, Ospald F, Kabel M (2016) Computational homogenization of elasticity on a staggered grid. *Int J Numer Methods Eng* 105:693–720.
- Collell J, et al. (2014) Molecular simulation of bulk organic matter in type II shales in the middle of the oil formation window. *Energy Fuels* 28:7457–7466.
- Laubie H, Radjai F, Pellenq R, Ulm F-J (2017) Stress transmission and failure in disordered porous media. *Phys Rev Lett* 119:075501.
- Montroll EW, Weiss GH (1965) Random walks on lattices. II. *J Math Phys* 6:167–181.
- Kenkre VM, Montroll EW, Shlesinger MF (1973) Generalized master equations for continuous-time random walks. *J Stat Phys* 9:45–50.
- Dentz M, Guze P, Russian A, Dweik J, Delay F (2012) Diffusion and trapping in heterogeneous media: An inhomogeneous continuous time random walk approach. *Adv Water Resour* 49:13–22.
- Lee SB, Kim IC, Miller CA, Torquato S (1989) Random-walk simulation of diffusion-controlled processes among static traps. *Phys Rev B Condens Matter* 39:11833–11839.
- Kalnin JR, Kotomin E (1998) Modified Maxwell-Garnett equation for the effective transport coefficients in inhomogeneous media. *J Phys Math Gen* 31:7227–7234.
- Kalnin JR, Kotomin EA, Maier J (2002) Calculations of the effective diffusion coefficient for inhomogeneous media. *J Phys Chem Solids* 63:449–456.
- Obliger A, Ulm F-J, Pellenq R (2018) Impact of nanoporosity on hydrocarbon transport in shales’ organic matter. *Nano Lett* 18:832–837.
- Fujita H (1993) Free volume interpretation of the polymer effect on solvent dynamics. *Macromolecules* 26:643–646.
- Hsu J-P, Lin S-H (2005) Diffusivity of solvent in a polymer solution-expansive free volume effect. *Eur Polym J* 41:1036–1042.
- Obliger A, et al. (October 23, 2018) Poroelectricity of methane-loaded mature and immature kerogen from molecular simulations. *Langmuir*, 10.1021/acs.langmuir.8b02534.
- Walsh JB (1981) Effect of pore pressure and confining pressure on fracture permeability. *Int J Rock Mech Min Sci Geomech Abstr* 18:429–435.
- Wang C, Wu YS, Xiong Y, Winterfeldt PH, Huang Z (2015) Geomechanics coupling simulation of fracture closure and its influence on gas production in shale gas reservoirs. *SPE Reservoir Simulation Symposium*. Available at <https://www.onepetro.org/conference-paper/SPE-173222-MS>. Accessed August 23, 2018.
- Wheaton R (2017) Dependence of shale permeability on pressure. *SPE Reservoir Eval Eng* 20:228–232.
- Striolo A, Cole DR (2017) Understanding shale gas: Recent progress and remaining challenges. *Energy Fuels* 31:10300–10310.
- Apostolopoulou M, Stamatakis M, Striolo A (2017) A kinetic Monte Carlo framework for multi-phase fluid transport in heterogeneous pore networks. *J Chem Phys* 147:134703.
- Backeberg NR, et al. (2017) Quantifying the anisotropy and tortuosity of permeable pathways in clay-rich mudstones using models based on X-ray tomography. *Sci Rep* 7:14838.

1 Supporting Information:

2 Mesoscale structure, mechanics, and transport properties of  
3 source rocks' organic pore networks

4 Jeremie Berthonneau<sup>1\*</sup>, Amaël Obliger<sup>1\*</sup>, Pierre-Louis Valdenaire<sup>1</sup>, Olivier Grauby<sup>2</sup>, Daniel  
5 Ferry<sup>2</sup>, Damien Chaudanson<sup>2</sup>, Pierre Levitz<sup>3</sup>, Jae Jin Kim<sup>4</sup>, Franz-Josef Ulm<sup>5</sup>, and Roland J.-  
6 M. Pellenq<sup>1,2,5</sup>

7  
8 <sup>1</sup>*<MSE>*<sup>2</sup>, the CNRS / MIT / Aix-Marseille University Joint Laboratory, Massachusetts

9 *Institute of Technology, 77 Massachusetts Avenue, Cambridge, MA 02139, USA*

10 <sup>2</sup>*Aix-Marseille Université, CNRS – UMR 7325 CINaM, campus de Luminy, Case 913, 13288*

11 *Marseille Cedex 9, France*

12 <sup>3</sup>*Université Pierre et Marie Curie, CNRS – UMR 8234 PHENIX, 75252 Paris cedex 5, France*

13 <sup>4</sup>*Shell International Exploration and Production Inc., Shell Technology Center at Houston, ,*  
14 *3333 Highway 6 South, Houston, TX 77082, USA*

15 <sup>5</sup>*Department of Civil and Environmental Engineering, Massachusetts Institute of Technology,*  
16 *Cambridge, MA 02139, USA*

17 *\*both authors contributed equally*

18

19

20

21

22

23

24 **Source Rock Samples.** This study was performed on three samples from economically  
 25 valuable source rock formations. The first one came from cuttings of the siliceous Marcellus  
 26 formation (MAR), Pennsylvania, USA. The second sample was extracted from the siliceous  
 27 Haynesville formation (HAY), Louisiana, USA. The last sample was mined from fresh  
 28 outcrops of the carbonaceous Lower Eagle Ford formation (LEF), Texas, USA. Their thermal  
 29 maturity (Table S1) was evaluated by RockEval pyrolysis and vitrinite reflectance (%VR<sub>0</sub>)  
 30 using standard organic petrology technique (1). The total organic carbon (TOC) content were  
 31 3.34 wt.% in HAY, 5.10 wt.% in MAR, and 7.27 wt.% in LEF. The modified Van Krevelen  
 32 diagrams illustrate the differences in hydrocarbon generation potentials in term of hydrogen  
 33 and oxygen indices (HI and OI, Fig. S1A) and S<sub>2</sub> peak versus TOC (Fig. S1B). In brief, LEF  
 34 is a source rocks entering the oil window (0.65 %VR<sub>0</sub>) whereas HAY and MAR are source  
 35 rocks in the dry gas window (2.00 and 2.20 %VR<sub>0</sub>, respectively).

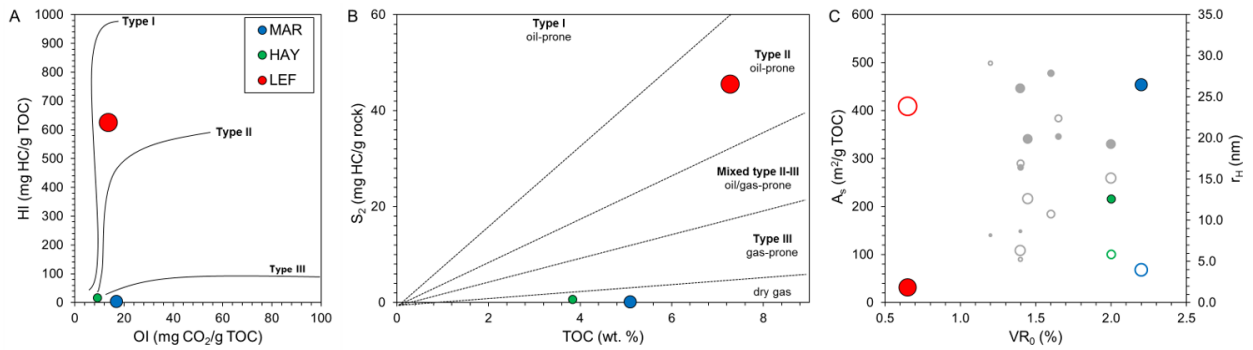
36

37 **Table S1.** Organic geochemistry of the studied source rocks from RockEval pyrolysis and  
 38 vitrinite reflectance. Hydrogen index (HI = S<sub>2</sub>/TOC x 100) and oxygen index (OI = S<sub>3</sub>/TOC x  
 39 100) were calculated from RockEval peaks S<sub>2</sub> and S<sub>3</sub>.

Sample	Total organic carbon <i>TOC</i> (%)	S <sub>2</sub> (mg HC/g rock)	S <sub>3</sub> (mg CO <sub>2</sub> /g rock)	HI (mg HC/g TOC)	OI (mg HC/g TOC)	Vitrinite reflectance <i>VRo</i> (%)
LEF	7.27	45.52	0.99	626.1	13.6	0.65
HAY	3.83	0.66	0.35	17.2	9.1	2.00
MAR	5.10	0.14	0.86	2.7	16.9	2.20

40

41 In addition, the organic matter (OM) contained in the oil-prone (LEF-OM) and one gas-  
 42 prone (MAR-OM) samples were isolated by acid demineralization with critical point drying  
 43 (2), and studied by RockEval pyrolysis. The TOC of these isolated OM samples were 36.3  
 44 wt.% in MAR-OM and 54.9 wt.% in LEF-OM.



46

47 **Figure S1.** Hydrocarbon generation potential and structural features of the studied source  
 48 rocks from bulk measurements. A: Pseudo van Krevelen diagram with hydrogen index (HI =  
 49 S<sub>2</sub>/TOC x 100) versus oxygen index (OI = S<sub>3</sub>/TOC x 100) evidencing the difference in  
 50 hydrocarbon generation potentials. B: Rock-Eval S<sub>2</sub> peak, quantifying the amount of  
 51 hydrocarbons released during the pyrolysis of kerogen, as a function of total organic carbon  
 52 content (TOC) allowing to infer on the oil-prone nature of LEF compared to the dry-gas  
 53 nature of HAY and MAR. C: Evolution of the porous media of the main North American  
 54 source rocks with respect to the thermal maturity. Surface area, A<sub>s</sub> (m<sup>2</sup>/g TOC, filled circles),  
 55 and hydraulic pore radius, r<sub>H</sub> (nm, open circles), from N<sub>2</sub> adsorption isotherms as functions of  
 56 thermal maturity as indicated by vitrinite reflectance, VR<sub>0</sub> (%). The grey symbols correspond  
 57 to results obtained on a large set of North American shale gas reservoirs (from ref. 3). The  
 58 three studied source rocks frame the general trends of increasing specific surface area and  
 59 decreasing pore radius with thermal maturity. The size of the symbols is proportional to the  
 60 TOC.  
 61

62 **Adsorption Isotherms.** Low pressure N<sub>2</sub> isotherms were performed on approximately 1.50  
 63 g of crushed source rocks, and 0.15 g of isolated OM at 77K using a Micromeritics 3Flex. The  
 64 samples were first degassed at 55°C under high vacuum in the apparatus to remove air, free  
 65 water, and other gases. The sorption measurements consisted in quantifying the gas uptake by  
 66 volume, as a function of pressure. The upper bound of the pressure during the experiment is  
 67 the saturation vapor pressure, P<sub>0</sub>. At low relative pressure (P/P<sub>0</sub> < 0.3) the analysis gas builds  
 68 up a monolayer on the surface. At higher relative pressures, a multilayer coverage takes place,  
 69 followed by gas condensation in the pores. The potential for capillary condensation is given  
 70 by the Kelvin equation:

$$71 \quad \ln\left(\frac{P}{P_0}\right) = \frac{-\gamma_{LV}V_L}{RTT_M} \quad (\text{SI-1})$$

72 where  $\gamma_{LV}$  is the liquid/vapor surface tension,  $V_L$  is the molar volume of the liquid,  $R$  is the  
73 ideal gas constant (J/mol/K),  $T$  is the temperature (K), and  $r_M$  is the average pore size, which  
74 was considered equivalent to the hydraulic radius ( $r_M \approx r_H = 4V_p/A_s$  (4)). The data were  
75 interpreted applying the multi-point Brunauer–Emmett–Teller (BET) theory for surface area  
76 ( $A_s$ ) calculation, and density functional theory (DFT) analyses for the determination of the  
77 pore volume ( $V_p$ ) and the pore size distribution (PSD). The DFT molecular model of N<sub>2</sub>  
78 adsorption at 77K on carbon slit pores was used as it provides an accurate approach for PSD  
79 determination of nanoporous materials (5).

80 The nitrogen adsorption isotherm of LEF at 77K shows a very low adsorption amount  
81 for reduced pressure  $P/P_0$  under 0.8. A small hysteresis loop is visible on the desorption  
82 branch at  $P/P_0 > 0.5$ . On the other hand, the isotherms of HAY and MAR display a noticeable  
83 amount of adsorption at  $P/P_0 < 0.05$  and hysteresis loops of the desorption branch at  $P/P_0 >$   
84 0.45, clearly indicating Type IV isotherms common for mature source rocks (4,6). The  
85 specific surface area,  $A_s$ , determined from the data corresponding to  $P/P_0 < 0.2$ , comes to 2; 7;  
86 and 23 m<sup>2</sup>/g (corresponding to 32; 189; and 454 m<sup>2</sup>/g TOC), for LEF, HAY, and MAR,  
87 respectively (*Table S2*). The average pore volume,  $V_p$  (for pore width < 185.8 nm) was  
88 measured at  $P/P_0 > 0.99$  and represented 0.0136; 0.0106; and 0.0230 cm<sup>3</sup>/g. Fig. S1C  
89 evidences the evolution of  $A_s$  (filled circles) as a function of the vitrinite index, VR<sub>0</sub>, for our  
90 samples together with those obtained on a large set of North American sources rocks (3). The  
91 BET surface areas ( $A_s$ ), pores volumes ( $V_p$ ), and hydraulic radii ( $r_H$ ) obtained from N<sub>2</sub>  
92 adsorption analysis are summarized in Table S2.

93 The isolated OM of LEF and MAR display similar N<sub>2</sub> adsorption isotherms than their  
94 respective parent source rocks (*Table S2*).  $A_s$  varies from 21 (LEF-OM) to 161 (MAR-OM)  
95 m<sup>2</sup>/g, which correspond to 38 (LEF-OM) and 443 (MAR-OM) m<sup>2</sup>/g TOC, in good agreement  
96 (within ~ 15 %) with those measured on the source rocks. The  $V_p$  measured on the isolated

97 OM (0.074 and 0.135 cm<sup>3</sup>/g for LEF-OM and MAR-OM, respectively) were however  
 98 significantly larger. PSDs of the isolated OM are illustrative of the change in pore structures  
 99 from the oil-prone to the dry gas-prone source rocks under investigation. MAR-OM exhibits  
 100 essentially a bimodal PSD with peaks in the range of 0.6-3.0 nm. LEF-OM displays a broad  
 101 distribution of pores with multiple modes between 5.0 and 100.0 nm.

102

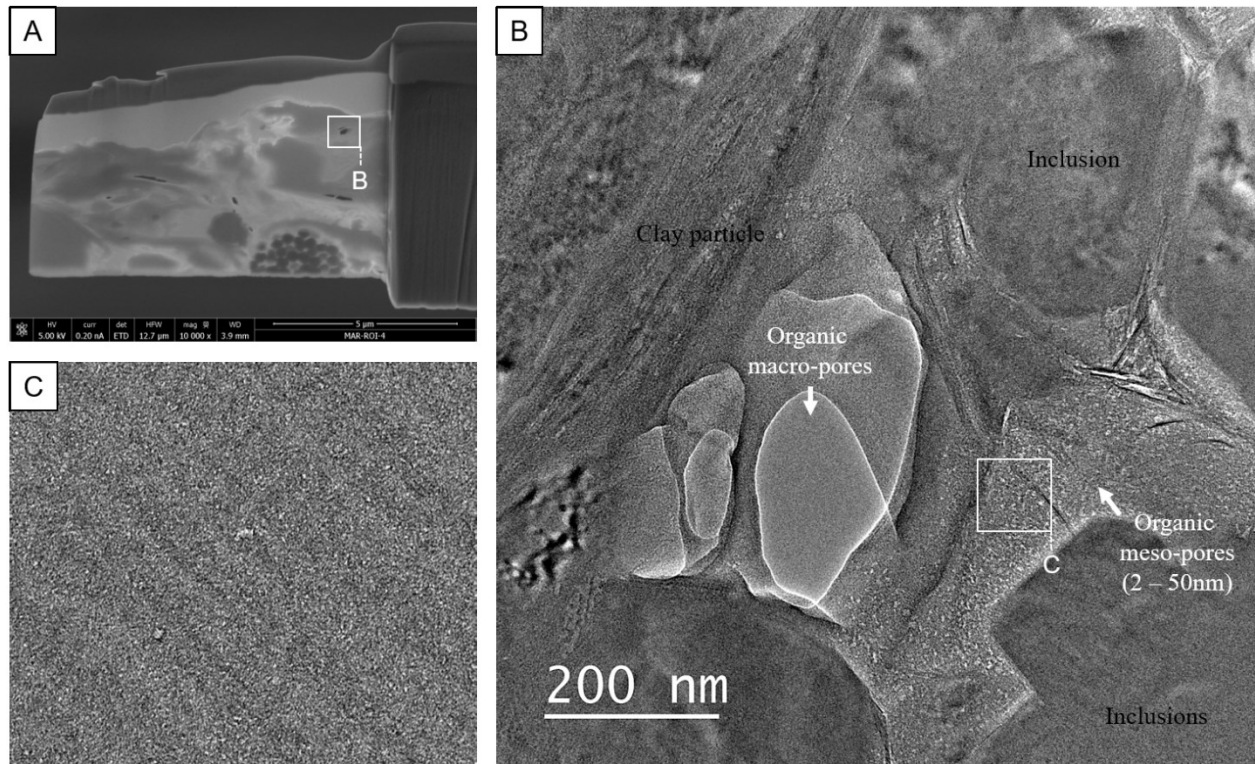
103 **Table S2.** Structural properties of the pores networks of the studied source rocks and isolated  
 104 OM from adsorption isotherms.

Sample	TOC	Specific surface area, $A_s$		Pore volume, $V_p$		Radius, $r_H$
	(%)	(m <sup>2</sup> /g)	(m <sup>2</sup> /g TOC)	(cm <sup>3</sup> /g)	(cm <sup>3</sup> /g TOC)	(nm)
LEF	7.27	2.28	31.36	0.014	0.187	23.9
HAY	3.83	7.22	188.51	0.011	0.277	5.9
MAR	5.10	23.13	453.53	0.023	0.451	4.0
LEF-OM	54.9	20.80	37.89	0.074	0.135	14.3
MAR-OM	36.3	160.89	443.22	0.135	0.371	3.3

105

106 **Electron Tomography.** Polished pieces of source rocks were subjected to a double flux of  
 107 Argon in a broad ion beam (BIB) milling machine for approximately four hours. The milled  
 108 samples were placed in a FEI Helios NanoLab 660 focused ion beam (FIB) where regions of  
 109 interest corresponding to migrated organic matter filling fossil cavities (LEF, and HAY) or  
 110 accumulated as a dense agglomerate (MAR) were identified. The migrated organic matter  
 111 (solid bitumen and/or pyrobitumen) is recognized as the main contributor of organic hosted  
 112 porosity (7,8). The last step consisted on extracting FIB thin sections from these organic  
 113 materials. The sections were thinned down to a thickness below 100 nm, allowing electron  
 114 transparency (9).

115 The produced FIB thin sections were studied with a transmission electron microscope  
116 (TEM, JEOL JEM 2011) fitted with a LaB<sub>6</sub> electron gun, under a 200 kV accelerating  
117 voltage. Conventional bright field imaging allowed to observe the hierarchical organic  
118 porosity of the studied source rocks (Figure S2).



119

120 **Figure S2.** Hierarchical organic porosity of MAR. A: Secondary electron micrograph  
121 (Everhart-Thornley Detector) of the FIB thin section extracted from the source rock sample.

122 B: Bright field TEM micrograph allowing distinction between mineral inclusions, clay  
123 particles, and organic matter (OM). OM displays both macro (> 50 nm) and meso (2 – 50 nm)  
124 pores. Only the organic mesoporosity were reconstructed in electron tomography (C).

125

126 The TEM is coupled with a single tilt axis geometry allowing for electron tomography

127 acquisition (10). Tilt series of bright field images were therefore collected on the organic

128 mesopores (Figure S2C) with a CCD camera (GATAN, Ultrascan® 1000XP) at a

129 magnification of 25, 000 (LEF) or 30, 000 (HAY, and MAR) over the range of  $\pm 40^\circ$  and

130 with an angular step of  $1^\circ$ . The range of achievable tilting angles was limited by the

131 shadowing effect of the FIB thin section edges. The acquisitions were assisted by the Digital

132 Micrograph software (GATAN).

133 The alignment of the stack of images composing the tilt series was performed in two  
134 successive steps with the TomoJ software (11): a fast translation correction based on cross  
135 correlations followed by a fine alignment based on 3D landmarks (local minima). The  
136 reconstruction of the aligned tilt series was achieved with the simultaneous iterative  
137 reconstruction technique (SIRT) using 30 iterations and a relaxation coefficient of 1 (11,12).

138 3D reconstructions from electron tomography usually display several artifacts which must  
139 be removed before further analysis (13-15). They condense as follow: side rays according to  
140 the minimal and maximal tilt angles ( $\theta$ ); side minima in the  $x$ -direction; and elongation of the  
141 features in the  $z$ -direction. A series of image processing treatments was thus performed on the  
142 reconstructions. First, the stacks of images were denoised by background suppression using a  
143 dedicated software (14). The produced series of background free images were then  
144 superposed to the reconstruction in order to find the optimal grey level at which the  
145 thresholding between the amorphous organic matter and the pore network maximizes fidelity.  
146 The binarized tomograms were then subjected to a Fourier angular filter in order to correct for  
147 elongation artifacts due to the significant missing wedge (15).

148 The final tomograms contain stacks of images with dimensions of  $252 \times 252 \times 66 \text{ nm}^3$   
149 (LEF),  $210 \times 210 \times 32 \text{ nm}^3$  (HAY), and  $210 \times 210 \times 21 \text{ nm}^3$  (MAR). Each voxel measures  
150  $0.42 \times 0.42 \times 0.42 \text{ nm}^3$  for LEF and  $0.35 \times 0.35 \times 0.35 \text{ nm}^3$  for HAY and MAR. The  
151 disordered nanoporous amorphous organic matter occupied the full volume of the tomograms.

152 A structural characterization of the tomograms was performed using the public-domain  
153 software iMorph (<http://imorph.fr/>) and imageJ. The pore size distribution (PSD) was  
154 determined using aperture map computation (16). At each point belonging to the pore phase,  
155 the size of the largest sphere containing pore voxels without overlapping with any solid  
156 voxels was determined. The aperture radius of such sphere was considered as the pore size.

157 The volumetric distribution of the aperture radii was used to obtain the granulometric  
158 distribution of this phase in the form of cumulative histograms.

159 The specific surface area was estimated from the chord length distribution (CLD) analysis  
160 (17-19). The CLD was obtained by propagating segments (chords) with random direction and  
161 from random origin points, hence producing an in-pore lengths histogram. The specific  
162 surface  $A_s$  was obtained from (19):

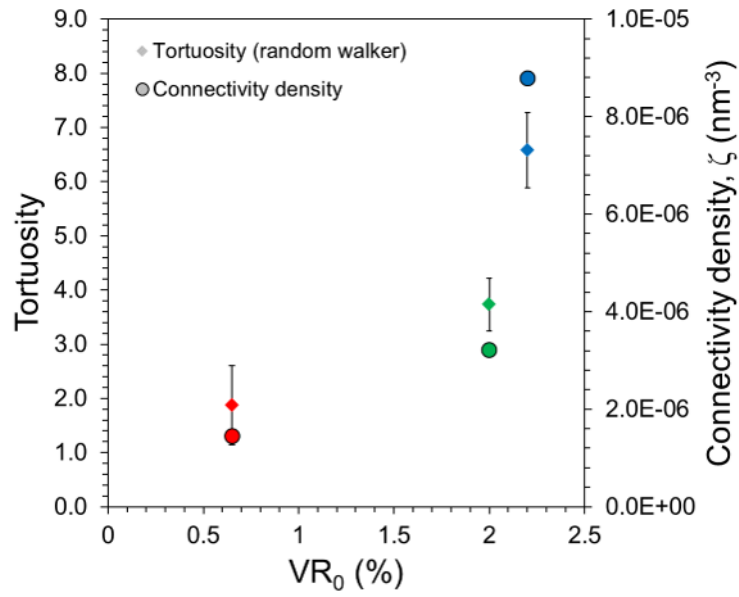
$$163 \quad A_s = \frac{4\varphi_{meso}}{\rho_s(1-\varphi_{meso})\langle\ell\rangle} \quad (\text{SI-2})$$

164 where  $\varphi_{meso}$  is the porosity of the tomogram,  $\rho_s$  is the density of the solid phase and  $\langle\ell\rangle$  is the  
165 first moment of the normalized CLD.

166 The tortuosity of the network was quantified by generating random walker within the pore  
167 network and recording their traveled free distance. To get the tortuosity, the mean free  
168 distance was divided by the Euclidian distance from the start point. In each case, 10,000  
169 random walkers were allowed to travel through the network during 300 iterations.

170 The pore network was then skeletonized using the script available within the BoneJ plugin  
171 (20). Eventually, the connectivity of the network was measured as the degree to which the  
172 pore structure is multiply connected, no matter the size and shape of the connections. This  
173 quantity reports the maximal number of branches that can be broken before the structure is  
174 separated into two parts, according to the method developed by (21). It allows one to extract  
175 the volume percentage of connected components sharing at least one pixel (percolation  
176 threshold,  $\chi = 0.42$  nm for LEF, and 0.35 nm for HAY and MAR), the first Betti number ( $\beta_1$ ),  
177 and the connectivity density corresponding to the ratio between  $\beta_1$  and the total volume of the  
178 tomogram ( $\zeta = \beta_1/V_t$ ).

179



180

181 **Figure S3.** Topological evolution of the organic porous networks highlighting the increases in  
 182 tortuosity and connectivity density,  $\zeta$  with respect to the thermal maturity (%VR<sub>0</sub>).  
 183

184

185 **Mechanical Properties.** A Fast Fourier Transform (fft)-based numerical model (22-24) was  
 186 used to compute the elastic response of LEF and MAR. To this end, we solve the mechanical  
 187 equilibrium at any point of the space, defined by  $\vec{r} = (r_1, r_2, r_3)$ , expressed by:

188 
$$\sigma_{ij}(\vec{r}) = C_{ijkl}(\vec{r})(\epsilon_{kl}(\vec{r}) - \epsilon_{kl}^*(\vec{r})); \frac{\partial \sigma_{ij}(\vec{r})}{\partial r_j} = \mathbf{0} \quad (\text{SI-3})$$

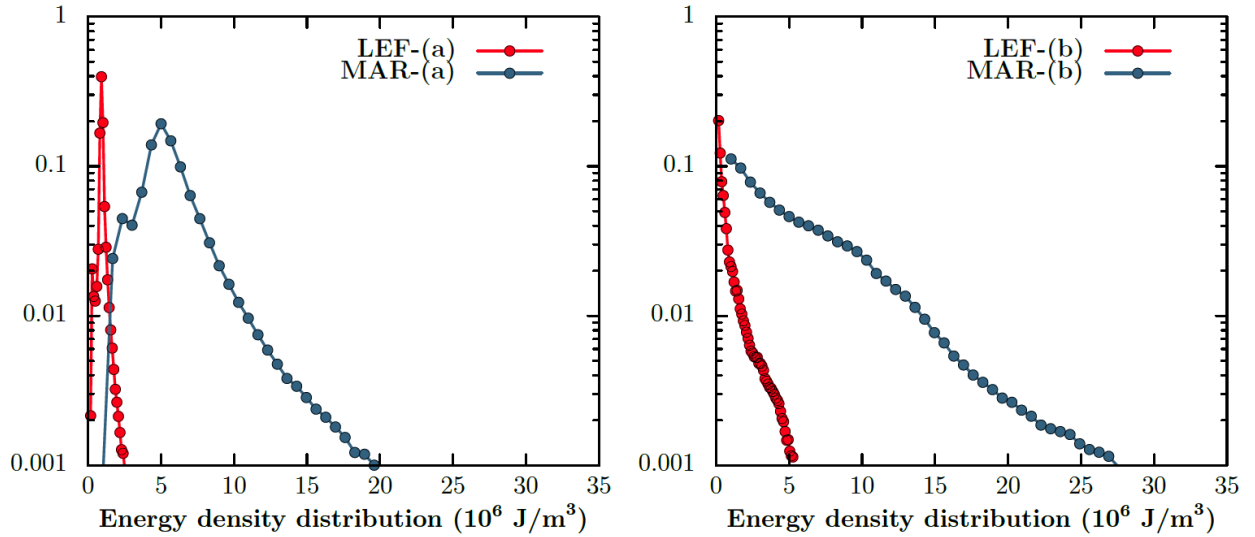
189 where the summation over repeated indices is assumed,  $C_{ijkl}(\vec{r})$  is the elastic stiffness tensor,  
 190  $\sigma_{ij}(\vec{r})$  is the stress tensor,  $\epsilon_{kl}^*(\vec{r})$  is the eigenstrain tensor which originates from pore swelling  
 191 and  $\epsilon_{kl}(\vec{r})$  is the total strain tensor. Eq. (SI-3) is solved by a fixed-point algorithm in Fourier  
 192 space requiring periodic boundary conditions, initially proposed by (22,23) and recently  
 193 improved by a variational scheme (24,25). This fixed point converged at  $10^{-7}$  following the  
 194 criterion on  $\epsilon$  in (25). We prepare two 700 x 700 mesostructures coming from cross-sections  
 195 at mid-distance of the small width of the two electron tomography reconstructions from LEF  
 196 and MAR. The local stiffness tensor,  $C_{ijkl}$ , of the organic phase is assumed isotropic. For both  
 197 mesostructures, we simulate two different agents. The first agent, called (a), is an imposed

198 averaged strain  $\langle \epsilon_{ii} \rangle = 0.01$ . As the algorithm operates with periodic systems, there is a  
199 topological misfit at the boundaries. The associated errors on the homogenized values are less  
200 than 1.1% compared to an homogenization performed on a centered 600 x 600 box. The  
201 second agent, called (b), is an adsorbed fluid inside pores, characterized by a fluid pressure  $P$ .  
202 Thus, in the pore phase, we impose  $\sigma_{ii} \sim P$ , and in the organic phase, we impose an  
203 eigenstrain,  $\epsilon_{ii}^* = \alpha_s \cdot P$ , accounting for the matrix swelling  $\alpha_s$ . Agent (b) has free strain  
204 boundary by adding a thin layer surrounding the nanostructure affected by 1% of the organic  
205 phase stiffness tensor. We take  $\alpha_s = 11.75 \times 10^{-3} \text{ GPa}^{-1}$ ,  $P = 8.8 \text{ MPa}$  for LEF and  $\alpha_s = 0$ ,  $P =$   
206  $40.1 \text{ MPa}$  for MAR. These pressures lead to the same averaged strain,  $\langle \epsilon_{ii} \rangle = 0.01$ , as with  
207 agent (a).

208 Under the two agents considered to compute the elastic response of the two  
209 mesostructures, the total elastic energy stored, reduced per volume unit ( $10^6 \text{ J/m}^3$ ), is 0.82 for  
210 LEF-(a), 0.9 for LEF-(b), 4.13 for MAR-(a) and 4.5 for MAR-(b). Whereas the total stored  
211 energy does not seem to vary with respect to the imposed agent, the respective energy  
212 distributions are radically different (Fig. S4). As seen on Fig. S4, agent (a) leads to Gaussian  
213 energy distributions whereas agent (b) leads to exponential energy distributions.

214

215



216

217 **Figure S4.** Energy density distribution resulting from the simulations of the two porous  
 218 structures originating from LEF (red) and MAR (blue) under two types of agent: a) imposed  
 219 strain boundary (left), and b) adsorbed fluid with free strain boundary (right).  
 220

221 **Transport Properties.** In this paragraph, we recall the Continuous Time Random Walk  
 222 (CTRW) numerical scheme on a lattice and the special treatment at the interface introduced to  
 223 account for sorption effects between the nanoporous and mesoporous phases. In a CTRW  
 224 process, the position and the travel time of the walkers at each step is updated as:

$$225 \quad \mathbf{r}_\alpha(\mathbf{n} + 1) = \mathbf{r}_\alpha(\mathbf{n}) + \mathbf{d}_\alpha(\mathbf{n}) \quad (\text{SI-4})$$

$$226 \quad \mathbf{t}_\alpha(\mathbf{n} + 1) = \mathbf{t}_\alpha(\mathbf{n}) + \mathbf{s}_\alpha(\mathbf{n}) \quad (\text{SI-5})$$

227 for the walker number  $\alpha$  where  $\mathbf{d}_\alpha(\mathbf{n})$  is a displacement from a lattice vertex to one of its first  
 228 neighbor chosen randomly among  $\pm \ell_x, \pm \ell_y$  or  $\pm \ell_z$  with equal probability  $w = 1/6$  ( $x, y,$  and  $z$   
 229 are the unitary vectors directing the lattice). Periodic boundary conditions are used in all  
 230 directions. Because there are different characteristic time scales in the system, the travel time  
 231 is also treated as a random variable and  $\mathbf{s}_\alpha(\mathbf{n})$  is the time spent by the walker  $\alpha$  at the position  
 232  $\mathbf{r}_\alpha(\mathbf{n})$ . This waiting time is chosen randomly according to the exponential distribution  
 233  $\exp(-s/\tau_i)/\tau_i$  so as to ensure the Fickian regime in the long time limit. The mean waiting  
 234 time  $\tau_i$  depends on the diffusion coefficients  $D_i$  of the phase  $i$  and are given as  $\tau_i = \ell^2/(6D_i)$ .  
 235 Additionally, if a random walker crosses an interface during a jump there is a probability  $\mathbf{1} -$

236  $\mathbf{p}(\mathbf{r}_\rho)$  (or  $p$  from the meso- to the nanoporous phase) to come back to its previous position.

237 This partial bounce-back step is introduced to enforce constant concentration in both phases at  
 238 equilibrium (26-28). The probability  $p$  is thus simply given by  $\mathbf{p} =$

239  $\rho_{meso}/(\rho_{nano} + \rho_{meso}) = \mathbf{r}_\rho/(\mathbf{1} + \mathbf{r}_\rho)$ . For a large number of walkers (several millions,  
 240 typically), we can compute the distributions of displacement  $\mathbf{P}_n(\Delta\mathbf{r})$  and of travel time

241  $\mathbf{I}_n(\Delta\mathbf{t})$  where the individual displacements and travel times are given by:

$$242 \quad \Delta\mathbf{r}_\alpha(\mathbf{n}) = \mathbf{r}_\alpha(\mathbf{n}) - \mathbf{r}_\alpha(\mathbf{0}) = \sum_{m=0}^{n-1} \mathbf{d}_\alpha(\mathbf{m}) \quad (\text{SI-6})$$

$$243 \quad \Delta t_\alpha(\mathbf{n}) = t_\alpha(\mathbf{n}) - t_\alpha(\mathbf{0}) = \sum_{m=0}^{n-1} s_\alpha(\mathbf{m}). \quad (\text{SI-7})$$

244 The Green function of the homogenized diffusion process is:

$$245 \quad \mathbf{G}(\Delta\mathbf{r}, \Delta\mathbf{t}) = \sum_{n=0}^{\infty} \mathbf{P}_n(\Delta\mathbf{r}) \mathbf{I}_n(\Delta\mathbf{t}) \quad (\text{SI-8})$$

246 In practice the summation can be done over 20000 timesteps to reach the Fickian regime. In  
 247 this case, the Green function converge to:

$$248 \quad \mathbf{G}(\Delta\mathbf{r}, \Delta\mathbf{t}) = \frac{1}{(4\pi\bar{D}\Delta\mathbf{t})^{3/2}} e^{-\Delta\mathbf{r}^2/(4\bar{D}\Delta\mathbf{t})} \quad (\text{SI-9})$$

249 from which we obtain the homogenized diffusion coefficient  $\bar{D}$ .

250 Here we detail the derivation of the model used in the manuscript eq. (3) and eq. (4).

251 When the Fickian regime is reached, after  $n$  walks, we can write the homogenized diffusion  
 252 coefficient as:

$$253 \quad \bar{D} = \frac{\langle \mathbf{r}(\mathbf{n})^2 \rangle}{2d(n_1\tau_1 + n_2\tau_2)} \quad (\text{SI-10})$$

254 where  $d$  is the number of dimensions,  $\mathbf{n}_1 = \mathbf{n}(\mathbf{1} - \varphi)\rho_{nano}/((\mathbf{1} - \varphi)\rho_{nano} + \varphi\rho_{meso})$  and

255  $\mathbf{n}_2 = \mathbf{n}\varphi\rho_{meso}/((\mathbf{1} - \varphi)\rho_{nano} + \varphi\rho_{meso})$  are the number of walks in the nano- and the

256 meso-porosity, respectively, and  $\langle \mathbf{r}(\mathbf{n})^2 \rangle$  is the average mean square displacement (msd) after

257  $n$  steps. We can rewrite these numbers as:

$$258 \quad \mathbf{n}_1 = \frac{n}{1+r_\varphi r_\rho} \quad (\text{SI-11})$$

259 
$$\mathbf{n}_2 = \frac{n r_\varphi r_\rho}{1 + r_\varphi r_\rho} \quad (\text{SI-12})$$

260 with the volume fraction ratio  $r_\varphi = \varphi / (1 - \varphi)$  and the concentration ratio  $r_\rho =$   
 261  $\rho_{meso} / \rho_{nano}$ . Because the waiting time and the displacement distribution probability for each  
 262 jump of the random walk process are decoupled, the average msd can be written as  $\langle \mathbf{r}(\mathbf{n})^2 \rangle =$   
 263  $n \mathbf{l}_{eff}^2$  where  $\mathbf{l}_{eff} = \gamma \ell$  is an effective hopping length that differs from the lattice spacing  $\ell$  to  
 264 a factor  $\gamma$  to take into account the sorption effect at the interface. Since there are additional  
 265 probabilities ( $p$  or  $1 - p$ ) for the random walker at the interface to bounce back to its previous  
 266 position, the average hopping length is lower than  $\ell$  and thus  $\gamma \leq 1$  where the equality arises  
 267 when there are no interfacial effects. This parameter can be seen as an obstruction factor that  
 268 captures the influence of the tortuosity as well as the sorption effects coming from the  
 269 different concentrations in both phases. Inserting this expression for the msd and eq. (SI-11)  
 270 and (SI-12) in eq. (SI-10) we obtain:

271 
$$\frac{\bar{D}}{D_{micro}} = \frac{1 + r_\varphi r_\rho}{1 + r_\varphi r_\rho r_D^{-1}} \gamma(r_\rho)^2 \quad (\text{SI-13})$$

272 where we have used the definition  $\tau_i = \ell^2 / (2dD_i)$  and  $r_D = D_{meso} / D_{nano}$ . We have  
 273 written the explicit dependence of  $\gamma$  on the concentration ratio  $r_\rho$  however it is also impacted  
 274 by the geometry of the system. The value of this parameter can be obtained simply by setting  
 275  $r_D = 1$ . In this case, a simple random walk simulation is enough since there is only one time  
 276 scale involved in the diffusion mechanism. To gain further insights into the impact of the  
 277 sorption effects on the upscaled diffusive properties we now turn to the derivation of a  
 278 specific model for the obstruction factor  $\gamma^2$ . For simplicity we will use the probability  $p =$   
 279  $r_\rho / (1 + r_\rho)$  instead of the concentration ratio  $r_\rho$ . First, we notice that when  $p = 0$  the  
 280 parameter  $\gamma^2$  is simply the obstruction factor of the nanoporous phase  $\gamma_0^2$  (or the inverse of the  
 281 diffusion tortuosity). When  $0 \leq p \leq 1$  (shortcut regime), most of the walkers will jump with an  
 282 average hopping length given by  $\gamma_0$  (in lattice unit) but some of those can take the mesopores

283 as shortcuts and conserve a hopping length of 1. The proportion of the random walkers taking  
 284 the shortcuts is proportional to  $p(1 - p)$  that is the probability of entering and exiting the  
 285 mesoporosity. Thus we can write  $\gamma^2 = \gamma_0^2 + Ap(1 - p)$  and then find a value for the constant  
 286  $A$  by imposing  $\gamma^2(p = 1/2) = 1$  which leads to  $A = 4(1 - \gamma_0^2)$ . We thus have:

$$287 \quad \gamma(p)^2 = f(p, \gamma_0) = \gamma_0^2 + 4(1 - \gamma_0^2)p(1 - p) \quad (\text{SI-14})$$

288 Additionally, this model recovers the proper limit  $\gamma^2 = 1$  when  $\gamma_0^2 = 1$  (i.e. when there is no  
 289 mesopore in the system). Since the limit of this model is  $\gamma_0^2$  when  $p = 1$  (perfect trapping  
 290 limit) which is unphysical, its validity is restricted to the shortcut regime ( $0 \leq p \leq 1/2$ ). To  
 291 extend this model beyond  $p=1/2$  we can conjecture by symmetry the behavior of  $\gamma^2$  in the  
 292 strong trapping limit ( $p \sim 1$ ), thus leading to  $\gamma^2(p \sim 1) \propto f(p, 0) = 4p(1 - p)$  and averaging  
 293 it with the previous model. We then have:

$$294 \quad \gamma(p)^2 = \frac{f(p, \gamma_0) + F(p, \gamma_0)f(p, 0)}{1 + F(p, \gamma_0)} \quad (\text{SI-15})$$

295 where the denominator is a normalization term and  $F(p, \gamma_0)$  a polynome of  $p$  with  
 296 coefficients depending on  $\gamma_0^2$  without loss of generality. This function should be chosen to  
 297 satisfy the limit  $\gamma(p)^2 = 1$  when  $\gamma_0^2 = 1$ . In the following we will restrict ourselves to the  
 298 leading order of this polynome. To ensure that  $\gamma(p)^2 = 1$  when  $\gamma_0^2 = 1$  we set  $F(p, \gamma) =$   
 299  $A^b p^c = [4(1 - \gamma_0^2)]^b p^c$  with  $b$  a positive real and  $c$  a positive integer. By setting  $b = 1/2$  and  
 300  $c = 3$  we recover eq. (3) of the manuscript. This choice gives very good agreements with the  
 301 numerical results (Fig. 3B of the manuscript). It should be emphasized that, due to the  
 302 averaging, the present model tends to  $\gamma_0^2 / \left(1 + 2\sqrt{1 - \gamma_0^2}\right)$  instead of zero in the strong  
 303 trapping limit ( $p \rightarrow 1$ ). Since this limit is, in practice, unlikely to be reached, we consider this  
 304 model as very robust. The largest value for  $p$  considered in the numerical study ( $\sim 0.833$ )  
 305 corresponds to a fluid concentration five times higher in the mesopores than in the

306 nanoporous phase. This situation can only occur for organic matter at unrealistically high  
 307 pressure even for very low intrinsic porosity of the nanoporous carbon phase.

308 In the following, we detail the models of diffusion coefficients and adsorption  
 309 isotherms we have considered for the microporous phase in MAR and LEF (Fig. 3C, main  
 310 text). In the case where the microporous matrix can be considered as rigid (MAR) the  
 311 diffusion coefficient is given as function of the loading and the porosity by

$$312 \quad D_s(\Gamma, \varphi) = \frac{k_B T}{n \xi_0^{\max}} \exp \left[ \alpha_0 (\varphi - \varphi_c) \left( \frac{1 - 2\beta_s \varphi \Gamma}{1 - \beta_s \varphi \Gamma} \right) \right] \quad (\text{SI-16})$$

313 where  $\xi_0^{\max} = 7.95 \cdot 10^{-12} \text{ N s m}^{-1}$ ,  $\alpha_0 = 8.57$ ,  $\varphi_c = 0.23$  and  $\beta_s = 0.64$  are constants  
 314 given for  $T = 423 \text{ K}$  (See ref. 29 for details). For MAR the porosity  $\varphi$  is 0.5, and the fluid  
 315 loading is given as function of the poessure by a Langmuir adsorption isotherm :

$$316 \quad \Gamma \equiv \frac{\rho}{\rho_{\max}} = \frac{\kappa P}{1 + \kappa P} \quad (\text{SI-17})$$

317 where the Henry's constant  $\kappa$  is  $0.066 \text{ Mpa}^{-1}$  for the Marcellus microstructure. We recall that  
 318 those models for diffusion and adsorption are obtained from molecular simulations using  
 319 realistic simulations of molecular structures of kerogens' microporosity (30,31).

320 For the numerical application of the mesoscopic model for the homogenized diffusion  
 321 coefficient with models of diffusion coefficient and adsorption isotherm in LEF, we have  
 322 chosen, in contrast to the MAR case, to account for flexibility effects that are very likely to  
 323 occur in an oil prone kerogen. Since swelling is neglected in the previous model of diffusion  
 324 in kerogens' microstructures, we have chosen a free volume theory of the Fujita type able to  
 325 account for adsorption induced swelling on the diffusion coefficient as function of the fluid  
 326 concentration :

$$327 \quad D_s(w) = D_0 \exp \left[ \alpha \left( \frac{\varphi_f(w) - \varphi_0}{\varphi_f(w) \varphi_0} \right) \right] \quad (\text{SI-18})$$

328 where  $D_0 = 0.77 \cdot 10^{-9} \text{ m}^2/\text{s}$  stands for the diffusion coefficient in the dilute limit ( $w \rightarrow 0$ ),  $\alpha =$   
 329 **11.4** is an adjustable parameter and  $\varphi_f(w) = V_{\text{free}}/V$  is the free volume ratio with  $V_{\text{free}}$  the

330 free volume inside the matrix at a given fluid quantity. Because of swelling, the free volume  
331 ratio increases with the fluid quantity  $w$  as

$$332 \quad \varphi_f(w) = \varphi_0 + \beta w \quad (\text{SI-19})$$

333 where  $\varphi_0 = 0.42$  is the porosity of the matrix with no fluid,  $\beta = 0.006255$  g/mmol with  $w$  in  
334 mmol of methane per gram of solid matrix. For this model (SI-18), the diffusion coefficient  
335 increases with the fluid concentration instead of decreasing due to the volume increase. For  
336 the adsorption isotherm, swelling is thought to extend the domain of validity of the low  
337 coverage linear regime to larger pressures. In our case, for  $P < 100$  Mpa, we simply have  
338  $w(P) = 14.14 P$ . The models (SI-18, SI-19) given here for the effect of swelling on  
339 adsorption and diffusion are not justified in the present study but are taken from an ongoing  
340 study. By analogy with diffusion of small penetrants into swellable polymers (32-34) one can  
341 consider it as a reasonable model for adsorption induced swelling effects for oil prone  
342 kerogens such as the LEF. It allows us to see how the mesoscopic model derived in this study  
343 behave with swelling effects on diffusion and adsorption.

344

#### 345 REFERENCES CITED

346

- 347 1. Taylor GH, Teichmüller M, Davis A, Diessel CFK, Littke R, Robert P (1998) *Organic*  
348 *petrology: A new handbook incorporating some revised parts of Stach's textbook of coal*  
349 *petrology* (Gebrüder Borntraeger, Berlin, Germany).
- 350 2. Suleimenova A, Bake KD, Ozkan A, Valenza II JJ, Kleinberg RL, Burnham AK, Ferralis  
351 N, Pomerantz AE (2014) Acid demineralization with critical point drying: A method for  
352 kerogen isolation that preserves microstructure. *Fuel* 135:492–497.
- 353 3. Clarkson CR, Solano N, Bustin RM, Bustin AMM, Chalmers GRL, He L, Melnichenko  
354 YB, Radlinski AP, Blach TP (2013) Pore structure characterization of North American

- 355 shale gas reservoirs using USANS/SANS, gas adsorption, and mercury intrusion. *Fuel*  
356 103:606–616.
- 357 4. Valenza II JJ, Drenzek N, Marques F, Pagels M, Mastarlerz M (2013) Geochemical  
358 controls on shale microstructure. *Geology* 41(5):611–614.
- 359 5. Do DD, Do HD (2003) Pore characterization of carbonaceous materials by DFT and  
360 GCMC simulations: a review. *Adsorption Science & Technology* 21(5):389–423.
- 361 6. Chen Q, Kang Y, You L, Yang P, Zhang X, Cheng Q (2017) Change in composition and  
362 pore structure of Longmaxi black shale during oxidative dissolution. *International*  
363 *Journal of Coal Geology* 172:95–111.
- 364 7. Bernard S, Wirth R, Schreiber A, Schultz H, Horsfield B (2012) Formation of  
365 nanoporous pyrobitumen residues during maturation of the Barnett shale (Fort Worth  
366 Basin). *International Journal of Coal Geology* 103:3–11.
- 367 8. Louks RG, Reed RM (2014) Scanning-electron-microscope petrographic evidence for  
368 distinguishing organic-matter pores associated with depositional organic matter versus  
369 migrated organic matter in mudrocks. *GCAGS Journal* 3:51–60.
- 370 9. Williams DB, Carter CB (1996) *The Transmission Electron Microscope* (Springer-Verlag  
371 US).
- 372 10. Franck J (2005) *Electron tomography: Methods for three-dimensional visualization of*  
373 *structures in the cell* (Springer-Verlag US).
- 374 11. Messaoudi C, Boudier T, Sorzano COS, Marco S (2007) TomoJ: tomography software  
375 for three-dimensional reconstruction in transmission electron tomography. *BMC*  
376 *Bioinformatics* 8(288), DOI: 10.1186/1471-2105-8-288.
- 377 12. Fernandez JJ (2013) Computational methods for materials characterization by electron  
378 tomography. *Current Opinion in Solid State and Materials Science* 17:93–106.

- 379 13. Biermans E, Molina L, Batenburg KJ, Bals S, Van Tendeloo G (2010) Measuring  
380 porosity at the nanoscale by quantitative electron tomography. *Nano Letters* 10:5014–  
381 5019.
- 382 14. Lottin D (2013) *Dimensions fractales, morphologie et caractéristiques dimensionnelles*  
383 *2D et 3D d'agrégats de nanoparticules de suie aéronautique : étude par microscopie*  
384 *électronique en transmission et tomographie électronique*. PhD Thesis, Aix-Marseille  
385 Université.
- 386 15. Kovacik L, Kerieche S, Höög JL, Juda P, Matula P, Raska I (2014) A simple Fourier  
387 filter for suppression of the missing wedge ray artifacts in single-axis electron  
388 tomography reconstructions. *Journal of Structural Biology* 186:141–152.
- 389 16. Vicente J, Wyart Y, Moulin P (2013) Characterization (two-dimensional–three-  
390 dimensional) of ceramic microfiltration membrane by synchrotron radiation: new and  
391 abraded membranes. *Journal of Porous Media* 16(6):537–545.
- 392 17. Mering J, Tchoubar D (1968) Interprétation de la diffusion centrale des rayons X par les  
393 systèmes poreux. I. *Journal of Applied Crystallography* 1:153–165.
- 394 18. Ioannidou K, Krakowiak KJ, Bauchy M, Hoover CG, Masoero E, Yip S, Ulm F-J, Levitz  
395 P, Pellenq RJ-M, Del Gedo E (2016) Mesoscale texture of cement hydrates. *Proceedings*  
396 *of the National Academy of Sciences* 113(8):2029–2034.
- 397 19. Pellenq RJ-M, Levitz P (2002) Capillary condensation in a disordered mesoporous  
398 medium: a grand conical Monte Carlo study. *Molecular Physics* 100(13):2059–2077.
- 399 20. Doube M, Klosowski MM, Arganda-Carreras I, Cordelieres FP, Dougherty RP, Jackson  
400 JS, Schmid B, Hutchinson JR, Shefelbine SJ (2010) BoneJ: Free and extensible bone  
401 image analysis in ImageJ. *Bone* 47(6):1076–1079.
- 402 21. Odgaard A, Gundersen HJG (1993) Quantification of connectivity in cancellous bone,  
403 with special emphasis on 3-D reconstructions. *Bone* 14:173–182.

- 404 22. Moulinec H, Suquet P (1995) A fft-based numerical model for computing the mechanical  
405 properties of composites from images of their microstructures. *IUTAM Symposium on*  
406 *Microstructure-Property Interactions in Composites Materials* 37:235–246.
- 407 23. Moulinec H, Suquet P (1998) A numerical method for computing the overall response of  
408 nonlinear composites with complex microstructures. *Computer Methods in Applied*  
409 *Mechanics and Engineering* 157(1-2):69–94.
- 410 24. Schneider M, Ospald F, Kabel M (2016) Computational homogenization of elasticity on a  
411 staggered grid. *Journal of the Mechanics and Physics of Solids* 105(9):693–720.
- 412 25. Valdenaire P-L (2016) *Crystal plasticity - Transport equation and dislocation density -*.  
413 PhD Thesis, Mines ParisTech.
- 414 26. Van Uem T (2009) Modified discrete random walk with absorption. *ArXiv*: 0903.0364.
- 415 27. El-Shehawey M A (2000) Absorption probabilities for a random walk between two  
416 partially absorbing boundaries: I. *Journal of Physics A: Mathematical and General* 33,  
417 9005.
- 418 28. Voter AF (2007) *Introduction to the kinetic monte-carlo method. In Radiation Effects in*  
419 *Solids*, NATO Science Series, 1–23 (Springer, Dordrecht).
- 420 29. Obliger A, Ulm F-J, Pellenq R (2018) Impact of nanoporosity on hydrocarbon transport  
421 in shales' organic matter. *Nano Letters*, 10.1021/acs.nanolett.7b04079.
- 422 30. Bousige C, Matei Ghimbeu C, Vix-Guterl C, Pomerantz AE, Suleimenova A, Vaughan  
423 G, Garbarino G, Feygenson M, Wildgruber C, Ulm F-J, Pellenq RJ-M, Coasne B (2016)  
424 Realistic molecular model of kerogen's nanostructure. *Nature Materials*, DOI:  
425 10.1038/NMAT4541.
- 426 31. Fujita, H (1993) Free volume interpretation of the polymer effect on solvent dynamics.  
427 *Macromolecules* 26: 643–646.
- 428 32. Fujita, H, Kishimoto, A (1958) Diffusion-controlled stress relaxation in polymers. II.

- 429            Stress relaxation in swollen polymers. *J. Polym. Sci.* 28: 547–567.
- 430    33. Hsu, J-P, Lin, S-H (2005) Diffusivity of solvent in a polymer solution-expansive free  
431            volume effect. *European Polymer Journal* 41: 1036–1042.
- 432    34. Kishimoto, A, Fujita, H (1958) Diffusion-controlled stress relaxation in polymers. III.  
433            Stress relaxation in a swelling polymer. *J. Polym. Sci.* 28: 569–585.
- 434